Supporting Information for
Nanoscale Kinetics of Amorphous Calcium Carbonate Precipitation in H_2O and D_2O

Peter D. Morris†, Ian J. McPherson†*, Gabriel N. Meloni and Patrick R. Unwin*
Department of Chemistry, University of Warwick, Coventry, CV4 7AL
*E-mail: ian.mcpherson@warwick.ac.uk, p.r.unwin@warwick.ac.uk

Contents
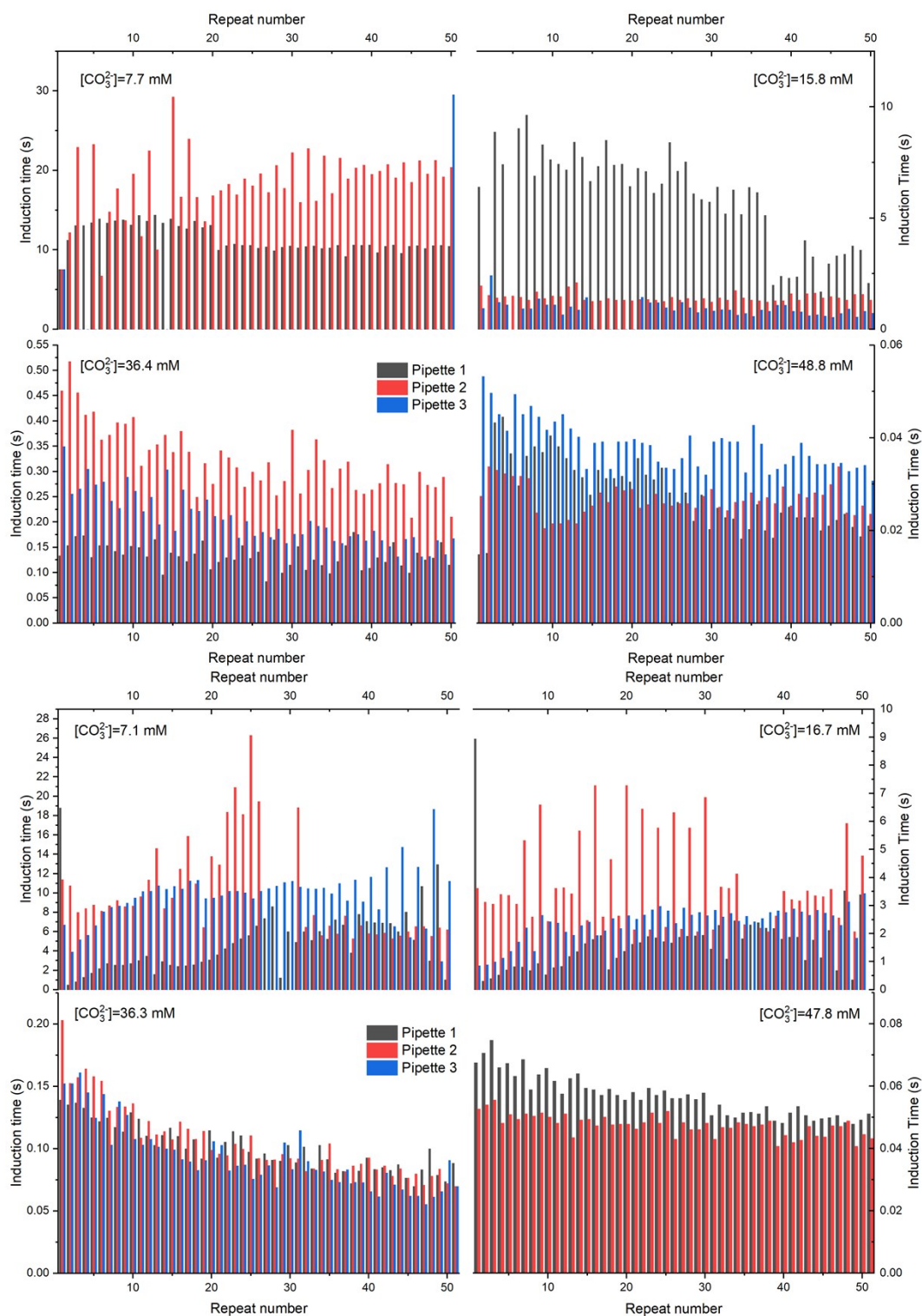
S1. Repeatability of induction time between runs

Figure S1: Induction times measured in H_2O (top 4 panels) and D_2O (bottom 4 panels) solutions. Data from the 3 replicate nanopipettes is shown (black, red, blue bars). One pipette at 7.7 mM CO_3^{2-} in H_2O and 47.8 mM CO_3^{2-} in D_2O failed to block entirely and so limited data is shown for these runs. Very occasionally no blocking event occurred on the timescale of a repetition and this is represented as an induction time of 0 s (but not included in any descriptive statistics).

S2. Preparation of H_2O and D_2O solutions of equivalent CO_3^{2-} concentration

To enable comparison of nucleation rates in H_2O and D_2O solutions effort was made to ensure the CO_3^{2-} concentration in each solution was comparable. Uncertainty surrounding the use of glass electrodes to make pD measurements prompted Raman spectroscopy to be explored as an alternative method for estimating the CO_3^{2-} concentration during solution preparation. The spectra of aqueous solutions of CO_3^{2-} is well studied,[1,2] including in D_2O solution,[3] and the peak intensities are known to increase linearly with concentration over the relevant range (0.01 – 0.1 M). The CO_3^{2-} concentration of each solution was therefore determined from the area of the fitted symmetric C-O stretching (a_1') band. This was observed at 1067 cm^{-1} (FWHM = 9.5 cm^{-1}) in H_2O solution and 1065 cm^{-1} (FWHM = 8.8 cm^{-1}) in D_2O solution (Figure S2A),[1,3] and was linear over the entire concentration range measured (3.125 mM – 100 mM, Figure S2B), consistent with previous reports.[3] To generate the calibration solutions sufficient NaOH (or NaOD) was added to a 100 mM Na_2CO_3 solution to ensure complete conversion to CO_3^{2-}, as determined from the absence of the ν(C-OH) band from HCO_3^- at 1016 cm^{-1}.[1] This provided the 100 mM calibration solution, which was then subject to serial dilution with H_2O or D_2O to generate 50, 25, 12.5, 6.25 and 3.125 mM solutions. The continued absence of the ν(C-OH) band in all spectra confirmed that dilution did not affect the speciation. A 4th order polynomial was fitted as a baseline and the a_1' band was fitted to a Voigt function to determine the band area. The area was then plotted as a function of concentration and fitted with a straight line to produce the calibration plot (Figure S2B). The method was validated using 3 repeat measurements from independently prepared H_2O solutions (Figure S2B, inset) which suggests measured concentrations have an uncertainty (95% prediction band, PB) of 3 mM.
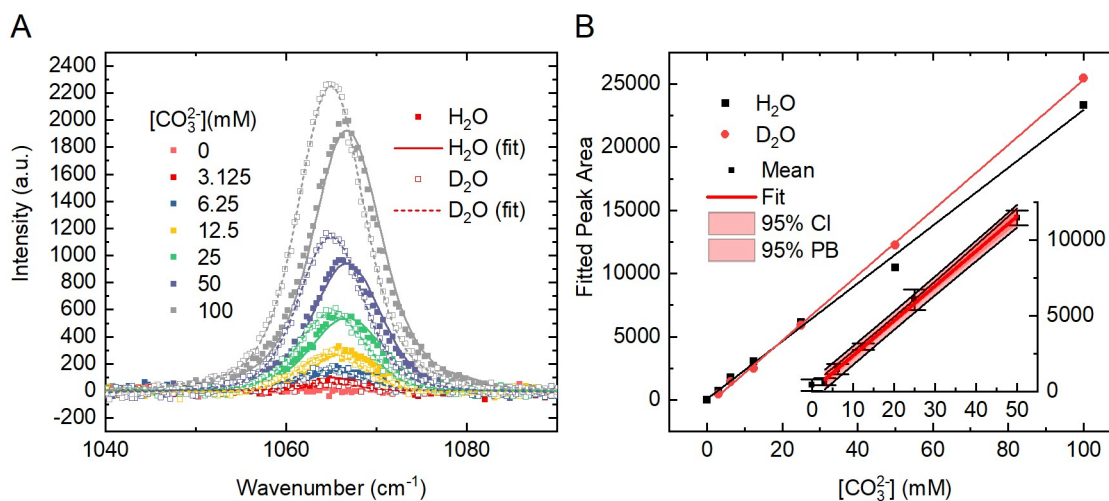

Figure S2: Calibration plots for the estimation of CO_3^{2-} concentration in H_2O and D_2O solutions from Raman spectroscopy. A: Baseline-subtracted experimental data (points) and Voigt fits (lines) for CO_3^{2-} concentrations between 0 and 100 mM in H_2O and D_2O. B: Fitted area as a function of concentration in H_2O and D_2O. Inset: Repeat measurements over range of interest with error bars showing 1 standard deviation and the 95% confidence band (CB) and 95% prediction band (PB).

A similar procedure was then used on the experimental solutions, with peak fitting used to separate the relative contributions of HCO_3^- and CO_3^{2-} to the spectrum. Example spectra showing these fits at two of the pH values are shown in Figure S3. Note the redshift of the ν(C-OH) band and appearance of the δ(COD) deformation band (1035 cm^{-1}) from HCO_3^- in

D_2O.[2] To account for variation in laser power (and therefore in absolute intensities) a new calibration was used each day, with later calibrations using 3 points. Concentrations predicted based on the three point calibrations were found to have a relative error of <±30% at the 95% confidence level.
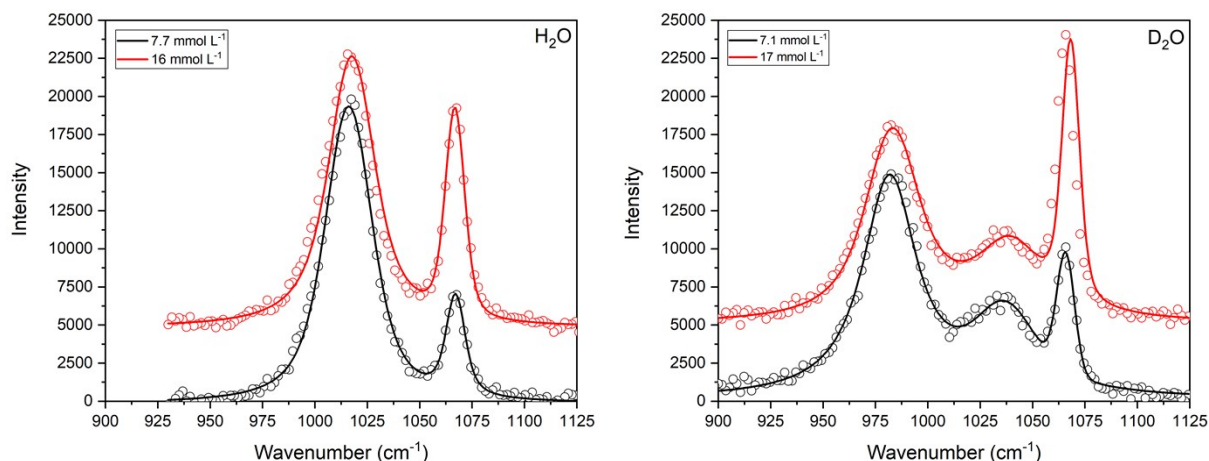

Figure S3: Raman spectra at different pH values. Left: Fitted spectra of two H_2O solutions of different carbonate concentrations. Right: Fitted spectra of two D_2O solutions of different carbonate concentrations, matched to the H_2O concentrations. In each case 2 (H_2O) or 3 (D_2O) Voigt functions (lines) were fitted to the experimental data (circles) to determine the CO_3^{2-} concentration.

S3. STEM images of Nanopipettes

Nanopipettes were imaged using scanning transmission electron microscopy (STEM). Due to the narrow wall thickness at the tapered end, this method is able to probe inside the nanopipette to a distance of several microns from the end. Control experiments reveal that in the absence of precipitation no significant contrast is observed inside the nanopipette, even when the nanopipette was filled with solution (Figure S4). Images of the nanopipettes used in the experiments reported in the main text are shown in Table 1. A lookup table was used to colour the images to highlight subtle variation in contrast. Absences in the table indicate instances where damage during retrieval or vacuum drying prevented imaging.
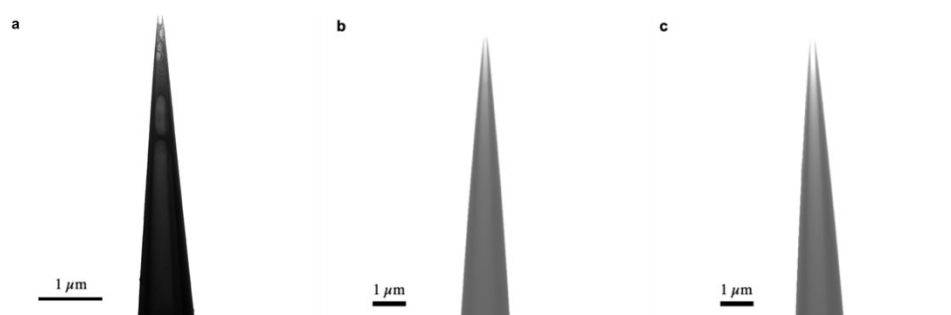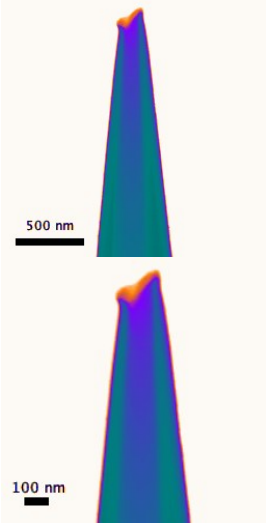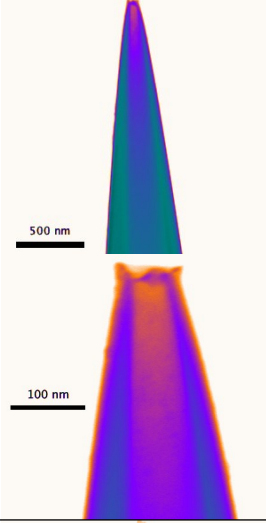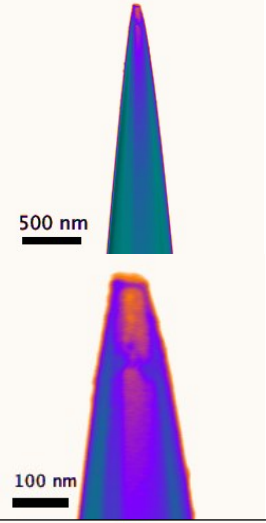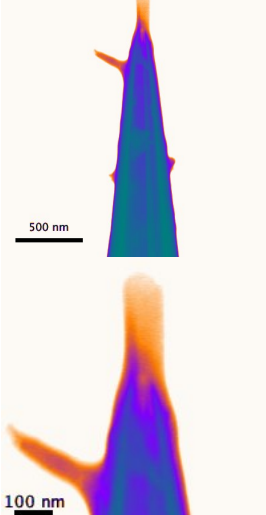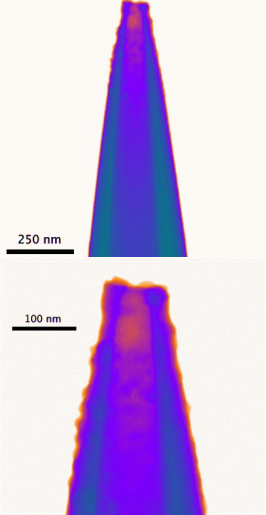

Figure S4: Three nanopipettes after being submerged in ethanol and freeze-dried. a) Example of a nanopipette where a precipitate has formed. b) Nanopipette that was filled with $NaHCO_3$ solution and submerged in $CaCl_2$ solution, but underwent no electrochemical mixing. c) Nanopipette that was not filled with or submerged in any solution.

Table S1 STEM images of nanopipettes following precipitation experiments

Tip Number	D$_2$O (7.1 mM)	H$_2$O (7.7 mM)
1		
2		
3		

Tip Number	D$_2$O (17 mM)	H$_2$O (16 mM)
1		
2		

Tip Number	D$_2$O (48 mM)	H$_2$O (49 mM)

1

2

3

S7
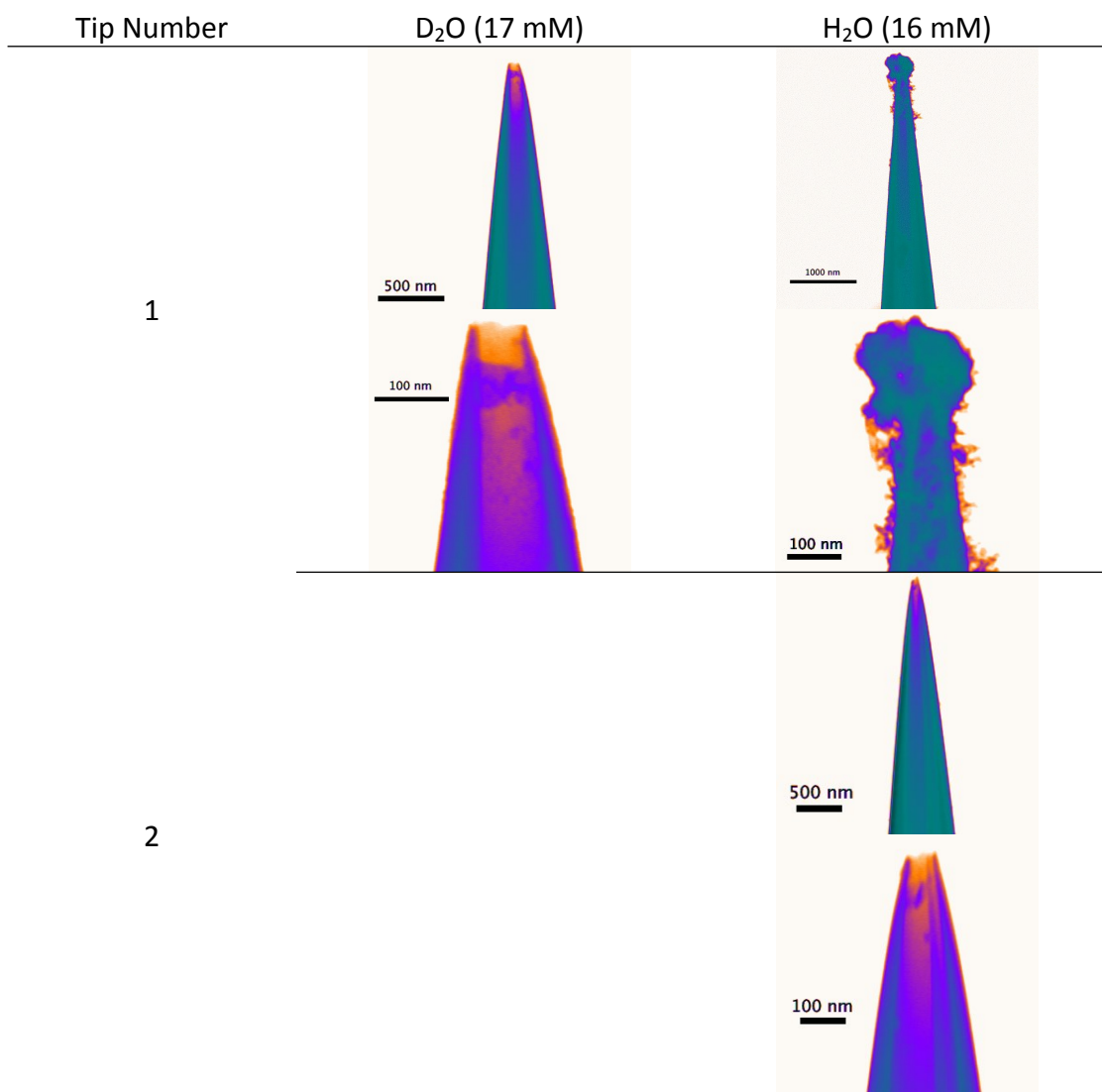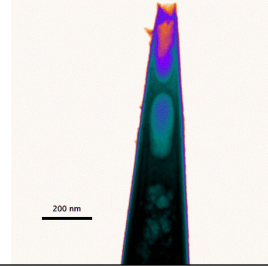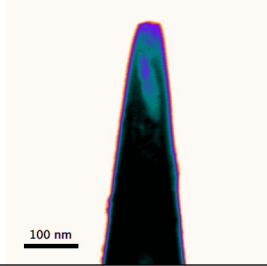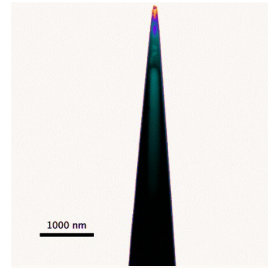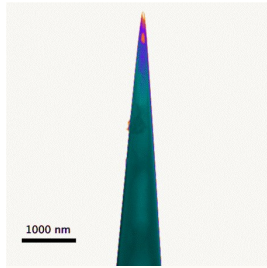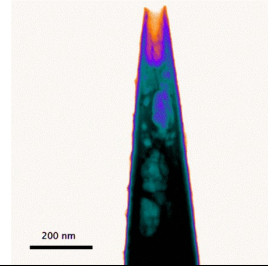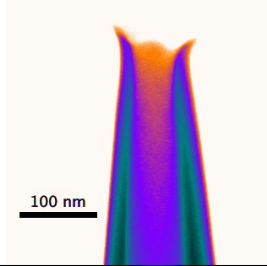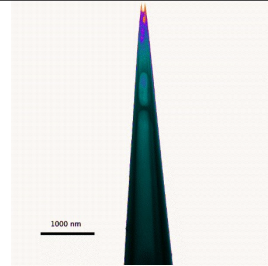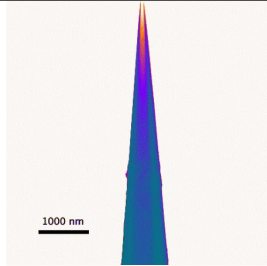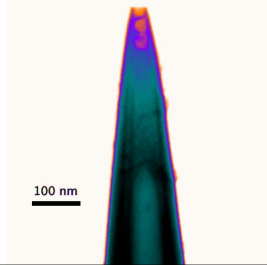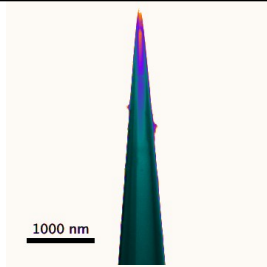
S4. Raman spectrum of nanopipette after precipitation
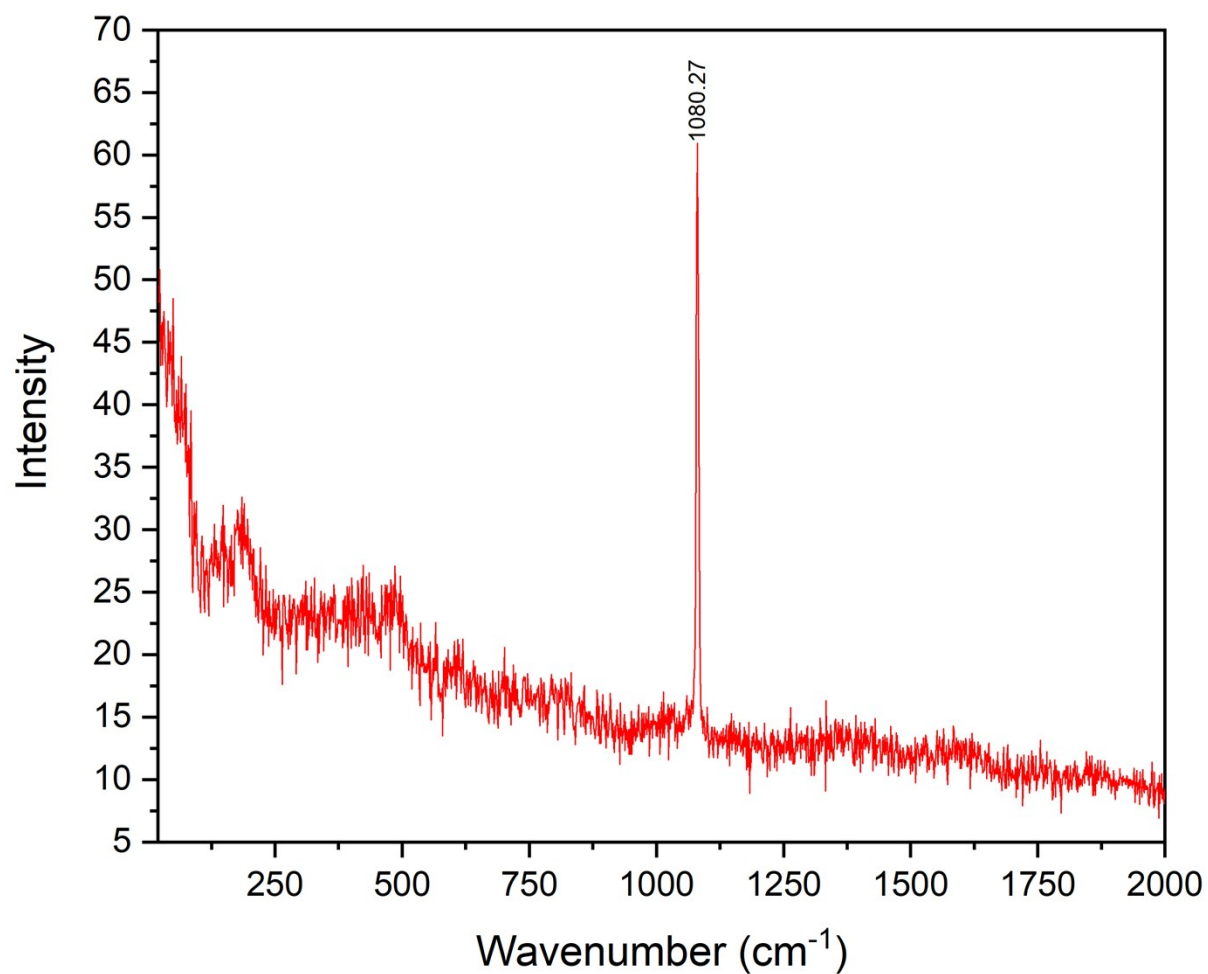
Figure S5: Raman spectrum of the end of a nanopipette after precipitation. Filling solution: $[CO_3^{2-}]$ = 48 mM, bath solution: $[Ca^{2+}]$ = 20 mM. Spectrum is the averaged result of 10 exposures of 2 s.

S5. Evaluation of the role of mass transport control in precipitation

To determine whether precipitation was controlled by kinetics or mass transport, the flux of Ca^{2+} was estimated from the total current and compared to the amount of Ca^{2+} ions estimated to form the ACC plug observed in STEM images (Figure S6). Given a conservative estimate of the Debye length under these type of conditions (0.96 nm for a 100 mM $NaHCO_3$ solution), and a conservative characteristic length scale of 15 nm (i.e. a pipette radius), the pipette walls should have little effect on the mass transport and conventional, rather than nanoscopic, mass transport can be considered.[4]
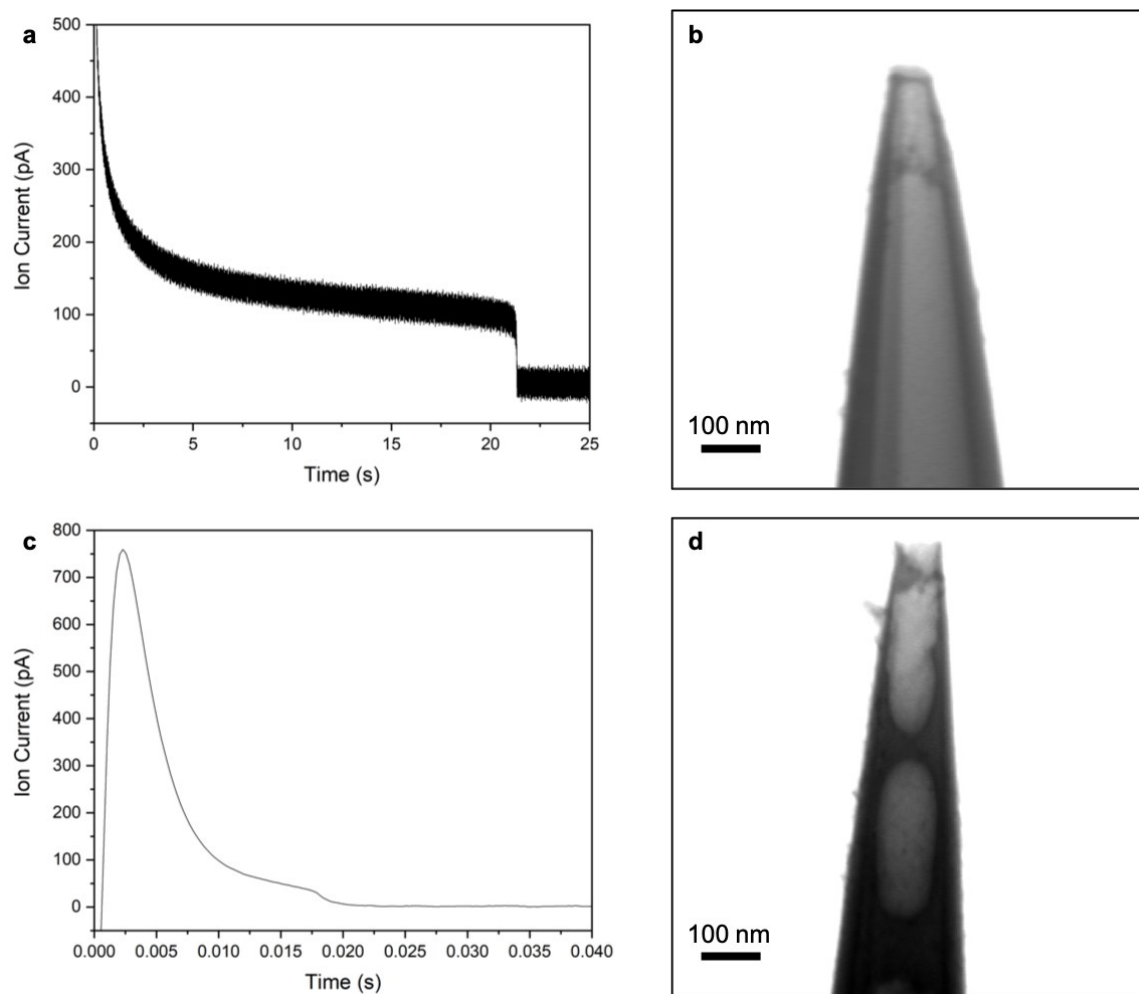
Figure S6: a) Current transient and b) STEM image of precipitate following blocking at $[CO_3^{2-}]$ = 7.7 mM (reproduced from Figure 2A, main text). c) Current transient and d) STEM image of precipitate following blocking at $[CO_3^{2-}]$ = 49 mM (reproduced from Tip 1, $[CO_3^{2-}]$ = 49 mM H_2O, Table S1 above).

The Ca^{2+} flux into the pipette, $j_{Ca^{2+}}$, can be estimated from the total current, i_{total}, and the transference number for Ca^{2+} in $CaCl_2$, $t_{Ca^{2+}}$, (Equations S1, S2) where F is Faraday's constant (F = 96 485 C mol^{-1}). At 25°C, in 20 mM $CaCl_2$ $t_{Ca^{2+}} = 0.42$.[5]

$$j_{Ca^{2+}} = \frac{i_{total} t_{Ca^{2+}}}{2F} \tag{S1}$$

S9

$$t_{Ca^{2+}} = \frac{i_{Ca^{2+}}}{i_{total}} \qquad\qquad (S2)$$

The total amount of Ca^{2+} transferred, $n_{Ca^{2+}}$, can therefore be found by integrating the current over the induction time and multiplying by the transference number (Equation S3).

$$n_{Ca^{2+}} = \frac{t_{Ca^{2+}}}{2F} \int_0^{t_{ind}} i_{total}(t)dt \qquad\qquad (S3)$$

By integrating the area under the curve shown in Fig S6a for $[CO_3^{2-}] = 7.7$ mM, (3.11×10^{-9} C) and using Equation S3, the value of $n_{Ca^{2+}}$ is 6.77×10^{-15} mol. The radius of the precipitate inside the nanopipette (Figure S6b, 42 nm) gives an approximate volume (assuming a sphere) of 3.13×10^{-22} m^3. From this, we can calculate the mass of the sphere (5.94×10^{-16} g) from the literature value of the density of ACC (1.9 g cm^{-3}),[6] and an assumed formula weight ($CaCO_3 \cdot H_2O$, 118 g mol^{-1}), the amount of Ca^{2+} within the plug is estimated to be 5.52×10^{-18} mol. This is significantly less than the number of ions being delivered to the nanopipette, indicating that the growth of ACC is not limited by mass transport, but is instead kinetically limited.

Repeating the above process for a system where $[CO_3^{2-}] = 48$ mM (shown in Figures S6c and S6d), where the charge passed is 4.04×10^{-12} C, yields $n_{Ca^{2+}} = 8.79 \times 10^{-18}$ mol – compared to the estimated amount of Ca^{2+} in the plug, 2.60×10^{-18} mol. These values are close, given the approximations involved, and in comparison to those of the $[CO_3^{2-}] = 7.7$ mM case, where there were three orders of magnitude difference between amount of Ca^{2+} in the volume of precipitate and the amount of Ca^{2+} being delivered. This suggests that the reaction tends towards being mass transport limited at higher pH values and faster induction times.

S6. Induction time data

Table S2 Induction times and derived nucleation parameters for the individual nanopipettes

[CO$_3^{2-}$] (mM) H$_2$O (D$_2$O)	Pipette	t_{ind} (s)						t_g (s)				$J \cdot V$ (m^{-3} s^{-1}·m^3)			
		H$_2$O	S.D.	N	D$_2$O	S.D.	N	H$_2$O	S.E.	D$_2$O	S.E.	H$_2$O	S.E.	D$_2$O	S.E.
7.7	1	11.2	2.28	51	4.873	3.308	50	9.048	0.561	1.215	0.121	0.336	0.107	0.272	0.013
(7.1)	2	18.4	4.14	49	9.907	4.945	46	8.964	1.346	4.320	0.110	0.061	0.075	0.215	0.006
	3				9.656	2.615	50			5.718	0.782			0.196	0.047
	Mean	14.8			8.145			9.006		3.751		0.1985		0.228	
	S.E.M	3.63			2.316			0.042		1.882		0.1375		0.032	
15.8	1	5.92	2.15	48	1.666	1.273	50	2.21	0.3	0.483	0.155	0.234	0.027	0.889	0.176
(16.7)	2	1.43	0.188	50	3.745	1.555	49	1.12	0.001	3.125	3.48	5.294	0.085	0.667	6.184
	3	0.95	0.326	43	2.381	0.582	50	0.534	0.011	1.037	0.286	3.689	0.219	0.595	0.19
	Mean	2.77			2.597			1.288		1.548		3.072		0.717	
	S.E.M.	2.24			0.863			0.694		1.138		2.111		0.125	
36.4	1	0.133	0.023	51	0.101	0.018	51	0.095	0.009	0.056	0.003	22	6	29	3
(36.3)	2	0.321	0.065	51	0.105	0.028	51	0.236	0.007	0.066	0	11	1	34	1
	3	0.202	0.051	51	0.093	0.026	51	0.141	0.003	0.077	0.002	16	1	59	7
	Mean	0.219			0.100			0.157		0.066		16.333		40.667	
	S.E.M.	0.078			0.005			0.059		0.009		4.497		13.123	
48.8	1	0.027	0.007	51				0.018	0.001			94	12		
(47.8)	2	0.027	0.003	51	0.057	0.007	51	0.022	0.002	0.047	0.001	188	88	168	43
	3	0.038	0.005	51	0.048	0.003	51	0.031	0.00	0.042	0.001	152	12	195	75
	Mean	0.031			0.052			0.024		0.044		145		164	
	S.E.M.	0.005			0.005			0.005		0.002		39		28	

S.D. = standard deviation, S.E. = standard error, S.E.M. = standard error of the means, N = number of events

S11

S7. Finite element method simulation of nanopipette mass transport

The model used to simulate the time dependent mixing of the nanopipette and bath solutions was similar to that reported previously.[7] An axisymmetric geometry was constructed based on a 50 µm spherical domain representing the bath, with the nanopipette geometry (based on STEM images) cut out (Figure S7). The model assumes speciation based on the PHREEQC database,[8] and considers the transport of the 12 most significant species (Table 3). Flux of the ith species, J_i, at concentration c_i, is calculated using the Nernst-Planck equation (Equation S4), while the electrical potential, V, satisfies the Poisson equation (Equation S5), where R is the molar gas constant (8.314 J K^{-1} mol^{-1}) and T is the temperature. Equilibria between the species (Table 4) are maintained by the continuity equation (Equation S6), where R_i is the reaction flux based on the forward and backward components of the equilibrium reaction with a suitable rate constant (Table 4). Equilibrium constants were based on the local species activity a_i (Equation S7), calculated from the activity coefficient γ_i based on the local ionic strength, I (Equation S8) using the Davies equation (Equation S9) with $A=1.82\times10^6$ $(\varepsilon T)^{-3/2}$. For charged species $b = 0.3$, for uncharged species $b = 0.1$.

$$j_i = - D_i\nabla c_i - z_i\frac{F}{RT}D_i c_i \nabla V \tag{S4}$$

$$\nabla^2 V = -\frac{F}{\varepsilon\varepsilon_0}\sum_i z_i c_i \tag{S5}$$

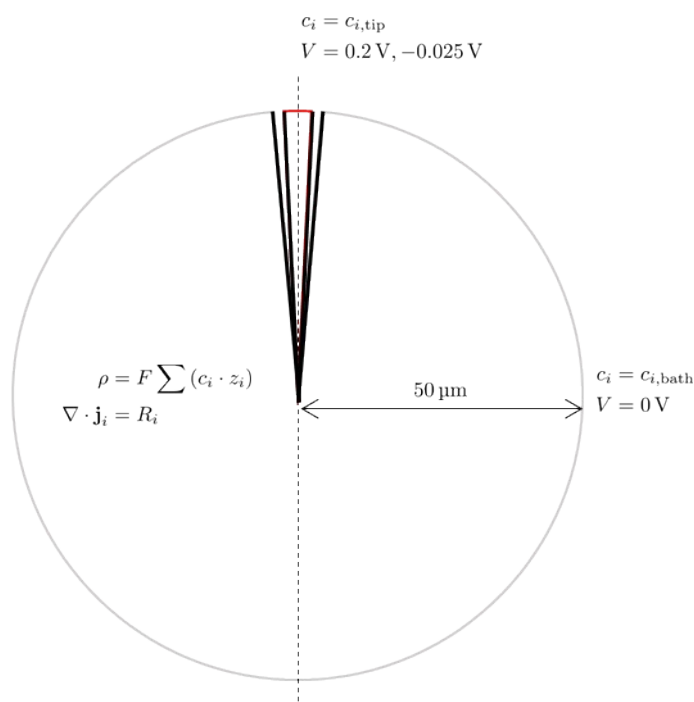$$\frac{\partial c_i}{\partial t} + \nabla\cdot j_i = R_i \tag{S6}$$

Figure S7: Illustration of the simulation domain used.

$$a_i = \gamma_i c_i \tag{S7}$$

$$I = \frac{1}{2}\sum z_i^2 c_i \tag{S8}$$

$$log_{10}\gamma_i = -Az_i^2\left(\frac{\sqrt{I}}{1+\sqrt{I}} - bI\right) \tag{S9}$$

Boundary concentrations were fixed at the equilibrium values determined for a 100 mM NaHCO$_3$ solution containing 1 µM CaCl$_2$ (nanopipette) or a 20 mM CaCl$_2$ solution containing 1 µM NaHCO$_3$ (bath). The inclusion of small amounts of the nanopipette/bath solution avoided zero values when determining equilibria. As the Raman measurement gave the total CO$_3^{2-}$ concentration (ΣCO$_3^{2-}$), both free and ion-paired, the effective pH of each solution was determined iteratively in PHREEQC to obtain self-consistent species concentrations. Initially the model was solved with the unblocking potential (+0.2 V) applied but without imposing the equilibrium fluxes. This solution was then used to provide the initial values for the model with equilibrium fluxes. A time dependent solution was then sought for the case with the blocking potential (-0.025 V) applied, using the unblocking potential solution as the initial value. The supersaturation, S, was evaluated over the whole model at each time point.

To evaluate the effect of D$_2$O on mass transport and supersaturation the following changes were made to the model. All diffusion coefficients were adjusted with the ratio D(H$_2$O) = 1.23 D(D$_2$O).[9] The dissociation constant for DCO$_3$ was taken to be 11.078 (pK_a^D = pK_a^H + 0.748).[10] The ionic product of D$_2$O was taken to be 0.154×10^{-14} (pK_w^D = 14.812).[11] The other equilibrium constants were not modified as the data were unavailable.

Table S3 Diffusion coefficients and boundary conditions applied in the FEM model

Species	D (10^{-5} cm^2 s^{-1})	Bath (mmol L^{-1})	Nanopipette (mmol L^{-1})			
ΣCO_3^{2-}			**7.67**	**15.79**	**36.51**	**49.06**
CO_3^{2-}	0.923	4.83×10^{-7}	4.55	9.25	20.87	27.64
$NaCO_3^{-}$*	1.2	3.81×10^{-12}	3.14	6.54	15.64	21.42
Ca^{2+}	0.792	20	4.14×10^{-4}	3.03×10^{-4}	1.93×10^{-4}	1.64×10^{-4}
Cl^{-}	2.05	40	2×10^{-3}			
Na^{+}	1.334	7.735×10^{-4}	101.3	106.3	118.6	125.8
H_2CO_3	1.92	1.71×10^{-4}	2.97×10^{-1}	1.23×10^{-1}	3.15×10^{-1}	1.54×10^{-1}
HCO_3^{-}	1.185	7.4×10^{-4}	89.02	81.25	61.15	49
H^{+}	9.311	1.628×10^{-4}	2.61×10^{-6}	1.20×10^{-6}	4.26×10^{-7}	2.65×10^{-7}
OH^{-}	5.273	9.43×10^{-5}	6.90×10^{-3}	1.53×10^{-2}	4.49×10^{-2}	7.37×10^{-2}
$NaHCO_3^{0}$*	0.673	2.09×10^{-10}	2.995	2.828	2.301	1.924
$CaHCO_3^{+}$*	0.506	1.13×10^{-4}	1.72×10^{-6}	1.12×10^{-6}	5.13×10^{-5}	3.38×10^{-5}
$CaCO_3^{0}$*	0.446	2.75×10^{-6}	4.14×10^{-4}	5.85×10^{-4}	7.56×10^{-4}	8.03×10^{-4}

* Taken from the updated Amm.dat database, originally calculated using the Pikal formula[8]

Table S4 Chemical equilibria considered in FEM model

Constants	Reaction	pK	k_b
K2 = kf2/kb2	$H_2CO_3 \rightleftharpoons HCO_3^{-} + H^{+}$	6.351	10^6 L mol^{-1} s^{-1}
K3 = kf3/kb3	$HCO_3^{-} \rightleftharpoons CO_3^{2-} + H^{+}$	10.330	10^6 L mol^{-1} s^{-1}
K4 = kf4/kb4	$Ca^{2+} + HCO_3^{-} \rightleftharpoons CaHCO_3^{+}$	-1.015	10^6 s^{-1}
K5 = kf5/kb5	$Ca^{2+} + CO_3^{2-} \rightleftharpoons CaCO_3^{0}$	-3.224	10^6 s^{-1}
K6 = kf6/kb6	$Na^{+} + CO_3^{2-} \rightleftharpoons NaCO_3^{-}$	-1.270	10^6 s^{-1}
K7 = kf7/kb7	$Na^{+} + HCO_3^{-} \rightleftharpoons NaHCO_3^{0}$	0.25	10^6 s^{-1}
Kw = kfw/kbw	$H_2O \rightleftharpoons H^{+} + OH^{-}$	13.997	10^9 L mol^{-1} s^{-1}

Table S5 Local flux of species from equilibrium reactions

Species, i	Reaction flux, R_i
Ca^{2+}	kb5([CaCO3]-K5[Ca][CO3])+kb4([CaHCO3]-K4[Ca][HCO3])
Na^{+}	kb6([NaCO3]-K6[Na][CO3])+kb7([NaHCO3]-K7[Na][HCO3])
H_2CO_3 (as CO_2)	kb2([H][HCO3]-K2[H2CO3])
HCO_3^{-}	kb2(K2[H2CO3]-[H][HCO3])+kb3([H][CO3]-K3[HCO3])+kb4([CaHCO3]-K4[Ca][HCO3])+kb7([NaHCO3]-K7[Na][HCO3])
CO_3^{2-}	kb3(K3[HCO3]-[H][CO3])+kb5([CaCO3]-K5[Ca][CO3])+kb6([NaCO3]-K6[Na][CO3])
H^{+}	kbw(Kw-[H][OH])+kb2(K2[H2CO3]-[H][HCO3])+kb3(K3[HCO3]-[H][CO3])
OH^{-}	kbw(Kw-[H][OH])
$NaHCO_3^{0}$	kb7(K7[Na][HCO3]-[NaHCO3])
$NaCO_3^{-}$	kb6(K6[Na][CO3]-[NaCO3])
$CaHCO_3^{+}$	kb4(K4[Ca][HCO3]-[CaHCO3])
$CaCO_3^{0}$	kb5(K5[Ca][CO3]-[CaCO3])

Examination of S after 10 s reveals that high values are only observed at the very tip of the nanopipette (Figure S8), justifying the size of the simulation domain. Closer examination of the tip region reveals the maximum supersaturation increases over the course of the first 100 ms, before stabilising. After this time, the supersaturated region then continues to expand up into the pipette, but not into solution, highlighting the more efficient mass transport into the nanopipette than out of it. The steady state supersaturation profile along the centreline of the nanopipette can also be examined (Figure S9d). The position of maximum supersaturation remains relatively similar for all four concentrations, occurring where the $Ca^{2+}:CO_3^{2-}$ ratio is close to 1.
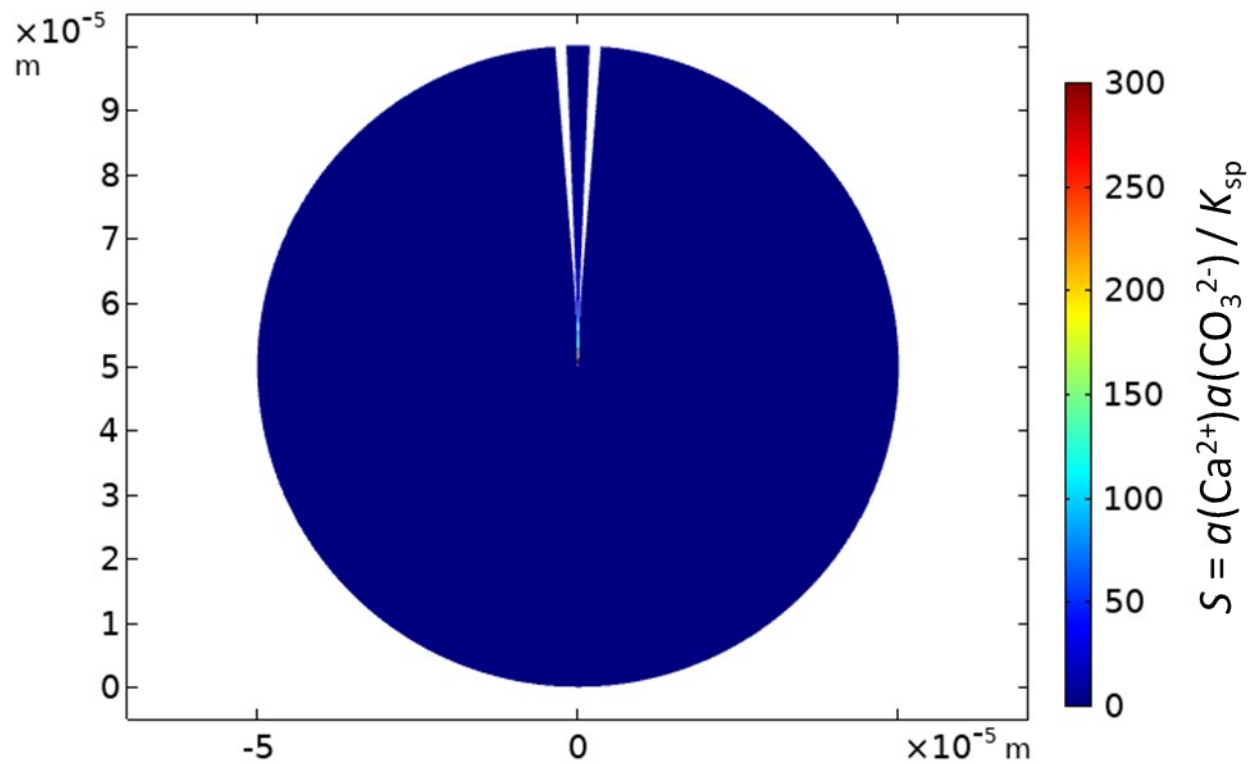

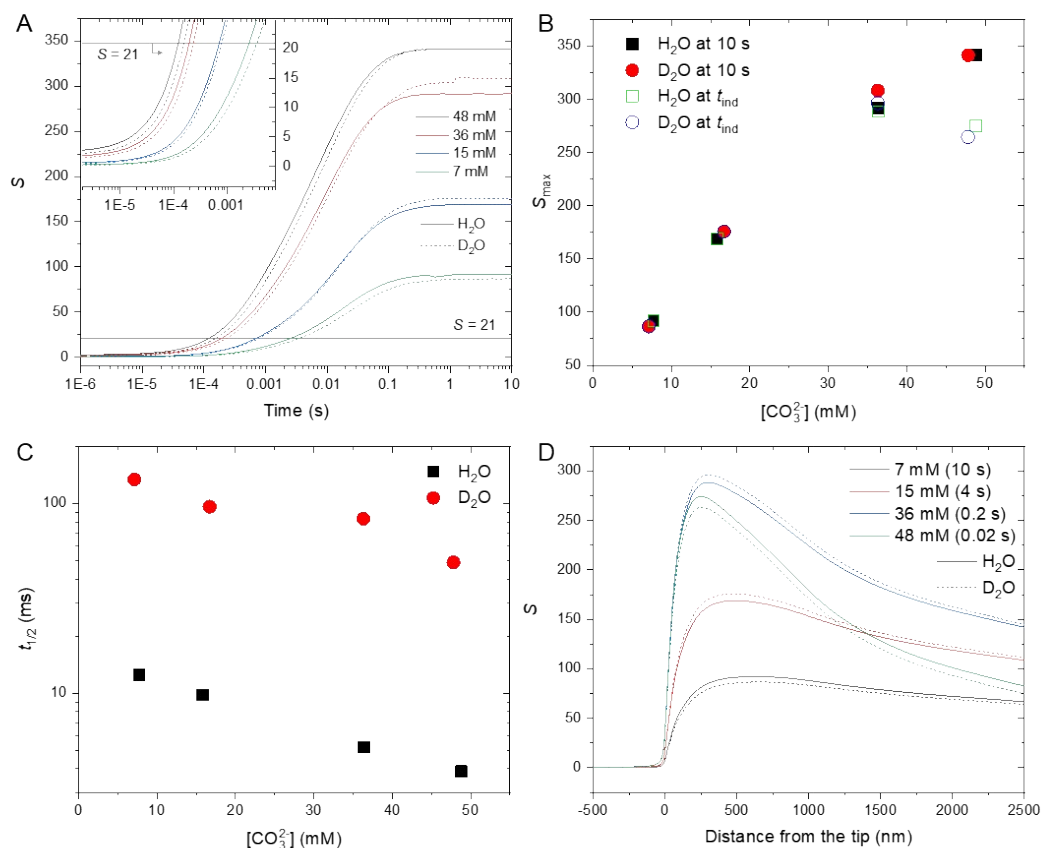Figure S8: Saturation calculated over the whole simulation domain after 10 s.

Figure S9: Simulated mixing of CaCl$_2$ and NaHCO$_3$ at the four CO$_3^{2-}$ concentrations of interest in H$_2$O and D$_2$O. (A) Time dependence of the value of maximum S. (B) Value of maximum S after 10 s (the length of the simulation, and at the observed t_{ind} (except 7 mM where 10 s is used again). (C) The half rise time, $t_{1/2}$, of S to its maximum value after 10 s. (D) The variation of S along the nanopipette axis at t_{ind}.
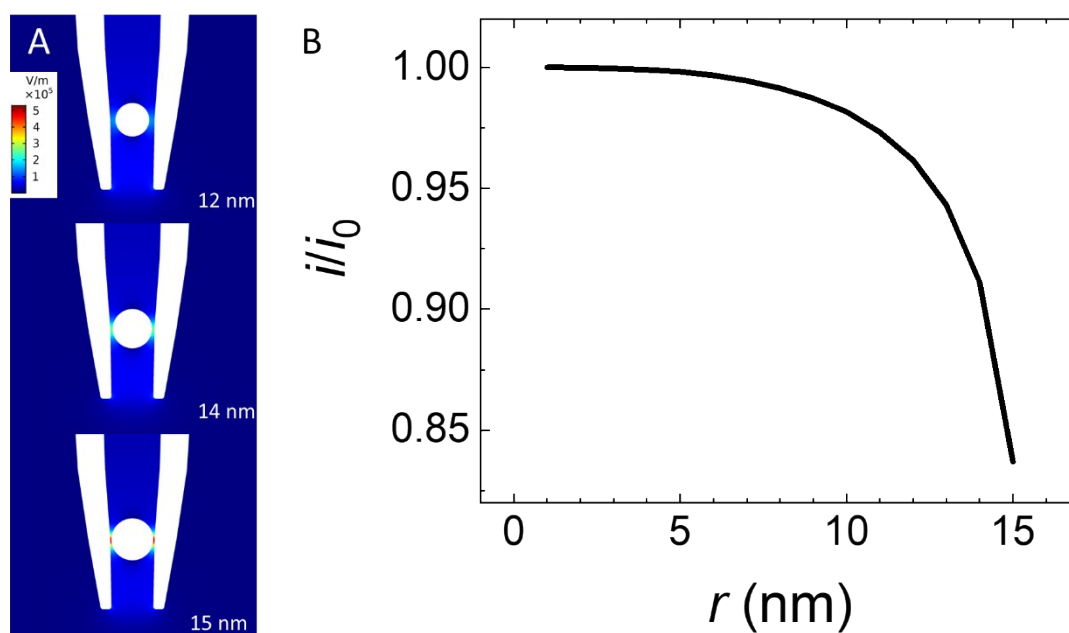
Figure S10: Effect of growing particle on the ion current in a nanopipette. (A) Magnitude of the electric field around particles of different radii (nanopipette radius at particle location is 15.75 nm) (B) Effect of particle radius on normalised current (relative to value for 1 nm particle).

S8. References

1 W. W. Rudolph, G. Irmer and E. Königsberger, *Dalton Trans.*, 2008, **0**, 900–908.

2 W. W. Rudolph, D. Fischer and G. Irmer, *Applied Spectroscopy*, 2006, **60**, 130–144.

3 B. G. Oliver and A. R. Davis, *Can. J. Chem.*, 1973, **51**, 698–702.

4 M. Tagliazucchi and I. Szleifer, *Materials Today*, 2015, **18**, 131–142.

5 A. G. Keenan, H. G. McLeod and A. R. Gordon, *The Journal of Chemical Physics*, 1945, **13**, 466–469.

6 F. Konrad, F. Gallien, D. E. Gerard and M. Dietzel, *Crystal Growth and Design*, 2016, **16**, 6310–6317.

7 D. Perry, A. S. Parker, A. Page and P. R. Unwin, *ChemElectroChem*, 2016, **3**, 2212–2220.

8 D. L. Parkhurst and C. A. J. Appelo, *Description of input and examples for PHREEQC version 3: a computer program for speciation, batch-reaction, one-dimensional transport, and inverse geochemical calculations*, Reston, VA, 2013.

9 P.-O. Gendron, F. Avaltroni and K. J. Wilkinson, *J Fluoresc*, 2008, **18**, 1093.

10 M. Paabo and R. G. Bates, *J. Phys. Chem.*, 1969, **73**, 3014–3017.

11 R. W. Kingerley and V. K. LaMer, *J. Am. Chem. Soc.*, 1941, **63**, 3256–3262.